Peach pit activated carbons: effect of raw material form and pyrolysis parameters for Hydrogen adsorption storage

Simone Bartucci, Carlo Poselle Bonaventura, Ludovica Pace, Giuseppe Conte, Giovanni Desiderio, Svetlana Mintova, Raffaele Giuseppe Agostino, Alfonso Policicchio

Peach pit activated carbons: effect of raw material form and pyrolysis parameters for Hydrogen adsorption storage

Simone Bartucci[1], Carlo Poselle Bonaventura[1], Ludovica Pace[4], Giuseppe Conte[1,3,*], Giovanni Desiderio[3], Svetlana Mintova[4], Raffaele Giuseppe Agostino[1,2,3] and Alfonso Policicchio[1,2,3,*]

[1]*Department of Physics, Università della Calabria, Via Ponte P. Bucci, Cubo 31C, 87036 Arcavacata di Rende (CS), Italy.*

[2]*CNISM - National Interuniversity Consortium for the Physical Sciences of Matter, Via della Vasca Navale, 84, 00146 Roma, Italy.*

[3]*CNR-Nanotec, c/o Università della Calabria, Via Ponte P. Bucci, Cubo 31C, 87036 Arcavacata di Rende (CS), Italy.*

[4]*Normandie Univ, ENSICAEN, UNICAEN, CNRS, Laboratoire Catalyse et Spectrochimie, Caen, 14000, France*

*Corresponding authors:

Tel. +39 0984 496095. Email: alfonso.policicchio@fis.unical.it (Alfonso Policicchio)

Tel. +39 0984 496158. Email: giuseppe.conte@unical.it (Giuseppe Conte)

Keywords: hydrogen adsorption, activated carbons, biomass, microporosity, NLDFT, pore size distribution, peach pit, prunus persica.

Abstract

The production of Activated Carbons (ACs) starting from economic precursors using eco-sustainable synthesis processes appears to be a particularly interesting research field. A possible application can be represented by the use of waste materials to produce ACs through synthesis processes with low environmental impact for hydrogen (H_2) storage.

In this work, ACs were produced starting from peach pits, through two processes, i.e. carbonization and physical activation of the raw material. The key process parameters (gas type and temperature) and the starting form of biomass have been modified to evaluate their influence on the structural properties and, consequently, the H_2 adsorption capacity. The chemical and morphological properties of the ACs were investigated through different analyses (Energy Dispersive X-ray - EDX, X-Ray Diffraction – XRD, Fourier-Transform InfraRed spectroscopy - FTIR, Scanning Electron Microscopy - SEM) while textural features and adsorption capacities were determined using volumetric apparatus. The optimization of the synthesis process allowed to obtain ACs with high microporous structure ($\simeq$ 85%), Specific surface area around 1317 m^2/g, Total Pore volume of 0.60 cm^3/g and excellent H_2 adsorption capacity at low pressure (1.85 wt% at 77 K up to 1 bar), interesting H_2 adsorption capacity at high pressure (3.45 $wt\%$ at 77 K up to 80 bar) and an excellent cyclicality of storage processes but reduced storage capacity at room temperature (0.28 $wt\%$ up to 80 bar).

1. Introduction

Currently, one of the most pressing problems the world is facing is climate change [1]. The demand for fossil fuels, especially coal, natural gas and oil has continued to grow very rapidly in recent decades causing a sharp increase in greenhouse gas emissions [2,3], mainly due to anthropic origin (industries, domestic use, traffic) and also to fire and disforestation of tropical forests [2,4]. Carbon dioxide concentrations, for example, have grown from 280 in 1780 to 415 ppm in 2019 in the northern hemisphere [5]. Associated with the increase of these greenhouse gases, many scientific studies highlight an increase in the earth's temperature [6–8] which is leading to extremely negative consequences for human beings, the ecosystems and biodiversity of the planet [9–12].

Then, in order to reduce the human impact on the environment and try to limit the possible irreversible damage caused by the use of fossil fuels, it is necessary to look for an alternative energy source, able to replace, at least partially, the use of fossil fuels [3,13,14]. New technologies, resources, and eco-friendly energy carriers are essential and encouraged to limit the release

of pollutants into the environment [15]. For all these reasons, H_2 is considered one of energy carrier of the future [16,17].

H_2 has a high energy per unit mass (142 MJ/kg) [18], about three times that of other fossil fuels [19]. However, it has a low volumetric energy density (0.01 MJ/L) [20] that does not allow storage in large quantities, it is also flammable and explosive [21].

It is essential to decrease the risks reducing the operating pressures of the tanks and, at the same time, increase the storage capacity in the same volumes to decrease management costs and overall dimensions [13,22,23].

An alternative and interesting method for H_2 storage is the sorption into solid materials able to retain H_2 at low pressures increasing safety and decreasing costs [20,24].

Materials that could represent a possible solution for these problems are nanostructured and nanoporous materials, such as MOF, zeolites, nanotubes, ZTC, porous polymers, mesoporous silicate materials, activated carbons and other carbon compounds [25]. ACs are interesting because they have several advantages among which certainly the ease of finding precursors, usually biomass [17]. The ACs production processes usually involve a series of steps. The raw material, before the carbonization/pyrolysis processes, it is subjected to dehydrating and/or homogenizing the grain size of the starting material.

According to the synthesis methodology used, it can be distinguished into: chemical [26] or physical activation [27].

The chemical activation is characterized by the impregnation of the precursor with dehydrating compounds: KOH, NaOH, H_3PO_4, etc. [26]. In this case, the obtained material requires a washing procedure to remove any remaining dehydrating agents [26].

The physical process, instead, occurs at higher temperature than the carbonization one step, in the presence of oxidizing gases such as water vapor, CO_2, or a combination of these [28].

In this work, for the synthesis of the ACs, only the physical activation process was taken into account: the choice of not using chemical substances allows an even more eco-sustainable process [29]. At the same time, evaluate the influence of the raw material form used on the porosity formation. The aim was to study how the granularity of the precursor, the type of gas used during the carbonization phase and the activation temperature modify the structural properties and the adsorption capacity of the synthetized ACs.

In particular, the purpose of this study is to determine the most suitable configuration of the synthesis parameters which allows to obtain the AC with the best performances, in terms of textural/structural properties and adsorption capacity. Therefore, the synthesized samples were investigated with volumetric-type techniques to analyze porosity and H_2 adsorption

capacity, and other morphological/structural study techniques (EDX, XRD, FTIR, SEM) were used, to correlate the structural properties to the amount of gas adsorbed as the pressure varies.

The optimization of the synthesis process has led to the production of highly microporous materials, which exhibit excellent structural properties such as high specific surface area and total pore volume, as well as H_2 storage capacity, both at low and high pressures, in addition to excellent reversibility and cyclicality of adsorption processes. Physical activation is the most probable method to achieve low-cost, low-pollution, green, sustainable, and large-scale industrial production of biomass porous carbon, particularly in the context of energy storage applications. [30]

2. Experimental section

The AC synthesized in this experimental work have been subjected to a process of carbonization and physical activation, starting from waste material, i.e. peach pits, derived from Prunus Persica purchased locally.

It is well known that the peach pit composition consists mainly of cellulose, hemicellulose, and lignin; in detail, it is composed of 46% cellulose, 14% hemicellulose, and 33% lignin [31].

The choice of peach pits as a precursor was due to several reasons. First, the environmental impact and eco-sustainability are central topics in this work, hence the idea is to recover waste materials and convert them into a new sustainable resource by applying a concept of circular economy [32]. Therefore, given in some cases the high production costs of commercial carbons, the use of waste materials/biomass allows the reduction of the impacts on the environment and cuts costs [33].

Furthermore, fruit pits pose a significant waste disposal problem for industries that process fruit. Literature shows that high-quality AC with low impurities and high adsorption capacities can be produced from fruit pits [34]. This consideration is behind the choice of the peach stones as precursor used for the production of AC.

Moreover, even in the procedure used for the production of the AC the eco-sustainability and environmental impact were considered selecting a physical activation rather than a chemical, which does not require the use of chemical solvents and washes [29,35–37].

2.1 Synthesis of AC derived from peach pit

The AC synthesis process was developed in the perspective of improving the structural properties and increasing H_2 storage capacity of the resulting samples. Initially, the optimization process concerned the granularity of the raw material. It is known that, not only the chosen synthesis process parameters can influence the characteristics and properties of the ACs produced, but also the initial form of the raw material plays a fundamental role [38]. In a second step, having determined the optimal granulation of the precursor, the optimization of the synthesis process concerned the physical parameters considered during the carbonization and activation phases.

The production process is performed in a furnace in which a stainless-steel sample holder is placed and linked to both a pipeline that provides the incoming gases (e.g. N_2, CO_2, etc.) flow and a drain pipeline. The furnace is made up of refractory material, able to withstand temperatures exceeding 1200 K, with electrical resistances that allow the internal temperature of the latter to be regulated with an accuracy of ±1°C, while the mass flow controller allows to regulate the gas flow in normal liters per minute. All the adjustable physical parameters of the system are controlled through a LabVIEW graphical interface (National Instrument) [39]. The raw materials were placed inside a ceramic crucible and subsequently entered in the cylindrical sample holder (dimensions: length 15 cm, internal diameter 5 cm).

Therefore, in a first stage starting from the same precursor (peach pit), several of AC samples using different starting forms were produced: whole shells, powdered shells and pelletized shells. The powders were obtained by treating the peach pits with a blender and a sieve, obtaining powders with grain size $\leq 0.5\ mm$, i.e. smaller than the size of the mesh holes of the sieve. A part of the powder material was then subjected to a pelletizing process, maintaining the samples at a pressure of 5000 kg/cm^2 for 5 minutes using a hydraulic press.

For all samples, the same synthesis process was carried out (see Table 2) to verify, under equal conditions, which was the most performing in terms of H_2 adsorption correlated to the best porous structure. In this stage, the carbonization process occurred in inert environment (N_2) while the activation process in an oxidizing environment (CO_2). More details on the carbonization and activation process are reported in the supporting information (See table S14).

After this pre-screening evaluation of the raw material form, the second stage was optimizing the synthesis process with the aim of improving the performance of selected types ACs

sample (the best precursor). In this case, the gas type in the carbonization step as well as activation temperature were varied to improve textural and adsorption properties. All the details on the parameters employed during the two-optimization stages and relative results have been reported in the section 3.

2.2 Characterization techniques

Very useful methods for optimization of ACs production are the thermogravimetric analysis (TGA) and Differential Thermal analysis (DTG) [40], performed to evaluate the mass loss and decomposition as a function of temperature [41], giving an insight of the temperature range required for production/synthesis of ACs materials [42]. These were carried out by using a Shimadzu DTG−60.

To obtain information on surface structural properties and chemical /atomic composition of the synthetized samples subjected to different carbonization and activation processes, Scanning Electron Microscopy (SEM) [43] and Energy Dispersive X-ray (EDX) analysis [44] were carried out by Quanta FEG 400 (FEI) while X-Ray Diffraction (XRD) analysis was carried out with a Rigaku Miniflex 600 equipped by Cu tube (40 kV, 30 mA), Fourier-transform infrared spectroscopy (FTIR) were performed on the raw material and on the synthesized ACs in the range from 3780-850 cm^{-1} [45]. All measurements were carried out using a Thermo Fisher Scientific Nicolet iS50 Fourier Transform IR Spectrometer equipped with a DTGS (DeuterTriglyceride Sulphate) detector. All the ACs samples (0.5 mg ± 0.1 mg) were made into KBr (100 mg ± 1 mg) pellets and prior the analysis have been treated at 373 K for 1 hour to removed the adsorbed water. To ensure the consistency of the data obtained, the FTIR spectra were post-processed using 'OMNIC' and 'Peakfit' evaluation software.

The sample's textural properties are evaluated from the adsorption/desorption isotherms of N_2 at 77 K up to 1 bar, while to quantify the storage capacity adsorption/desorption isotherms of H_2 at 77 K and at room temperature up to 1 bar have been acquired. Furthermore, on the best sample, isosteric heat of adsorption , reversibility and cyclicity up to 80 bar at 77 K and at room temperatures have been evaluated.

All the measurements up to 1 bar were performed using a Micromeritics ASAP 2460 while the high pressure measurements were carried out using the f-PcT (fast Pressure–concentration–Temperature) volumetric apparatus [46].

Before each adsorption/desorption measurement, all samples were outgassed at temperature of 473 K for 12 h under vacuum (10^{-5} mbar) to eliminate the eventual fraction of water weakly bound inside the samples.

The application of the Brunauer-Emett-Teller (BET) model [47] for the N_2 adsorption isotherms at liquid nitrogen temperature in the range 0.01-0.30 of relative pressure P/P0 allowed to determine the SSA values relating to each ACs [47]. Using the Non Local Density Functional Theory (NLDFT) [48], considering slit-shaped pores with energetically heterogeneous and rough walls [49], the values of Total Pore Volume (V_T) [50] and Pore Size Distribution (PSD) [51] were obtained distinguishing among ultra-micropores (V_{ult}), ultra-micropores (V_{sup}), micro-micropores (V_{mic}), meso-micropores (V_{mes}) [52].

The use of the Toth model and its related equation on the H_2 adsorption isotherms data, allows to extrapolate information such as the maximum asymptotic storage capacity, i.e. $wt\%_{MAX}$, and the degree of homogeneity of a surface, i.e. the parameter t [53].

3. Results and discussion

3.1 Raw material: preliminary analyses on peach pit

To understand how the carbonization/activation process influences the chemical and structural properties of the surface of the ACs produced, different preliminary analyzes were carried out on peach pits: 1) EDX analyzes were performed to evaluate the surface chemical composition and compare with that of the synthesized ACs; 2) FTIR analyzes were carried out to study the functional groups and evaluate how they change following the carbonization and activation processes; 3) TGA analyzes were carried out to relate the mass loss to which the samples are subjected during the synthesis process with the temperature; 4) XRD measurement were performed to evaluate structural composition checking for possible crystalline structure.

All analyzes were carried out on whole peach stone, not subjected to any type of physico-chemical treatment.

3.1.1 EDX analysis

To investigate the surface chemical properties of peach pits, EDX analyzes were performed on different area of the sample. Four different EDX analyses of the sample surface were acquired

(see Tables S1-S4). Elemental analysis of raw material in term of weight and atomic concentration is reported in Table 1.

Table 1: Chemical composition of raw material. The quantities reported represent the average values between all the measurements carried out.

	RAW MATERIAL	
Element	**Avg. wt. %**	**Avg. at. %**
C	68.05	73.98
O	31.80	25.95
K	0.13	0.03

Accordingly, to chemical analysis it is possible to state that the raw material contained Carbon, Oxygen, and a small percentage of potassium.

3.1.2 FTIR analysis

The surface functional groups of the raw material were characterized by FTIR analysis. Figure 1a shows the IR spectrum in the range of 850-1850 cm^{-1} and the range between 2650 and 3780 cm^{-1} is shown in Figure 1b. In both figures the main chemical bonds of the functional groups are identified.

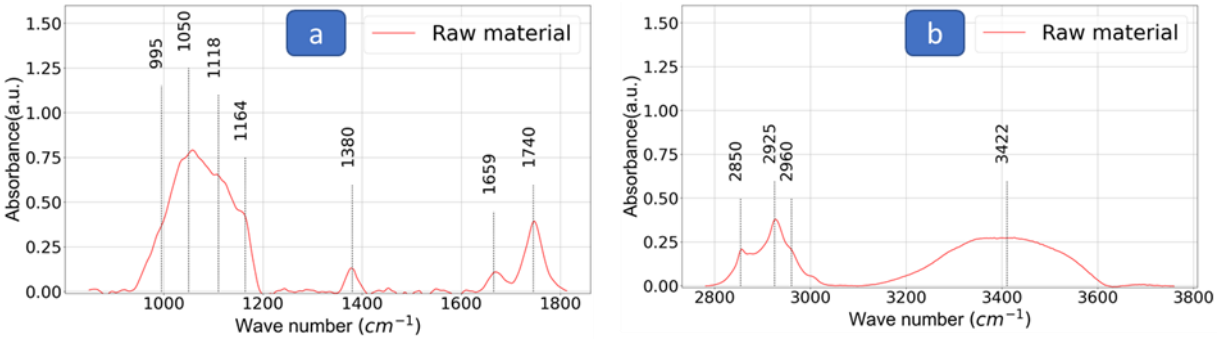

Figure 1: a) FTIR spectrum of raw material in the range of 850-1850 cm^{-1}; b) FTIR spectrum of raw material in the range of 2650-3780 cm^{-1}.

In Figure 1, the band at 1740 cm^{-1} corresponds to C=O stretching vibrations of carbonyl groups, such as carboxylic, aldehydes, esters and ketone groups in the structure [54].

The weak peak at 1659 cm^{-1} corresponds to a C=C stretching [55], while the one at 1380 cm^{-1} corresponds to the C–O stretching vibration [56]. The bands at 1164 cm^{-1} and 1118 cm^{-1} are attributed to phenol or alcohol vibrations (C-O-C), and aromatic C-H in-plane deformation [57]. The peak at 1050 cm^{-1} corresponds to the C–O bond [54]. Looking at Figure 1b, the presence of a band at 3422 cm^{-1} is assigned to O–H stretching vibration in hydroxyl groups, while the peaks

at 2960, 2925 and 2850 cm^{-1} are attributed to C–H stretching vibration of the aliphatic structures (alkenes and alkyl groups) [58].

3.1.3 TGA and DTG analysis

TGA analysis were carried out in inert (i.e. N_2) and oxidizing (i.e. air) environment conditions. The obtained results allowed to understand the behavior of peach shell at high temperatures before the physico-chemical treatment, to determine the temperature' limit for the syntheses, and to determine the initial mass to be carbonized in order to obtain a significant quantity of ACs [39]. A temperature rate of 5 K/min was set bringing the precursors from room temperature up to 1173 K (see Figure 2a,b).

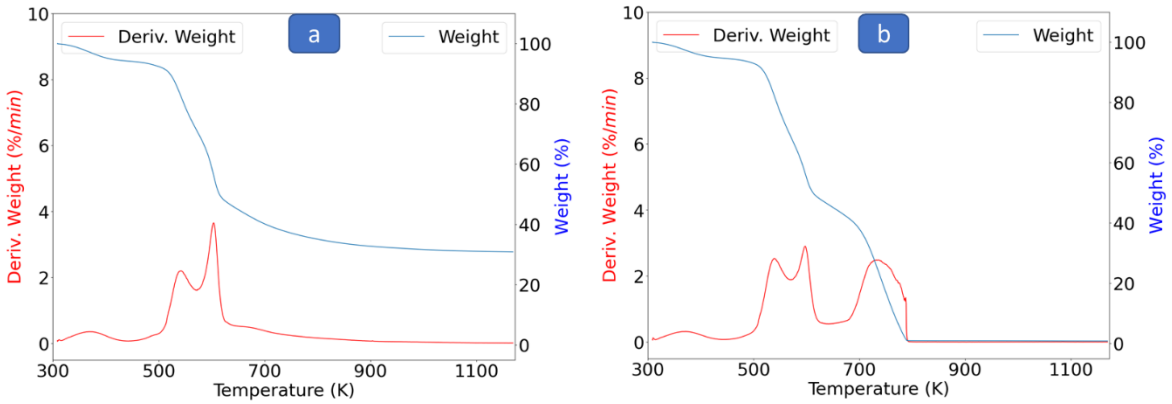

Figure 2: a) Thermogravimetric analysis of raw material in inert environment (N_2); b) Thermogravimetric analysis of raw material in oxidant environment (Air). For both measurements the key parameters are the following: Temperature rate: 5 K/min; Flux: 100 ml/min.

Looking at Figure 2a,b it is noticeable that, increasing temperature up to 1173 K, while in an inert environment the mass loss it is only 69%, on the contrary, it reaches value around 99% in an oxidizing one.

3.2 Optimization of the precursor: influence of the pre-treatment

To produce ACs samples using peach pits, starting precursor was considered as it is (whole shells) and in other two different forms (powder and pellet) (see Section 2.1), then subjected to carbonization and activation processes. In Table 2 the criteria used for naming the samples and all key parameters applied during the pyrolysis are reported.

Table 2: Samples nomenclature and key pyrolysis parameters. The acronym assigned to the samples uses the information from columns 2, 3, 4 and 5 only.

Sample name	Raw	Form	Carbonization	Carbonization	Activation	Activation	Activation

	material		Gas	range (K)	temperature (K)	Gas	time (min)
PPAC_WS_N2_1173	PPAC (Peach Pit ACs)	WS (Whole Shell)	N_2	673 - 1173	1173	CO_2	60
PPAC_POW_N2_1173	PPAC (Peach Pit ACs)	POW (Powder)					
PPAC_PEL_N2_1173	PPAC (Peach Pit ACs)	PEL (Pellet)					

By varying the form of the precursor and keeping the same experimental conditions (chosen based on literature data and previous research activities on similar materials)[36] for the three different types, the goal was to understand which precursor has well developed porosity.
At the end of the synthesis procedure, the ACs samples obtained showed mass loss higher than 80% (as reported in Table 3). The higher value compared with the one determined by the TGA analysis of **Erreur ! Source du renvoi introuvable.**, it is due to the fact that in addition to the inert gas N_2, also CO_2, which is much more aggressive, was also used on the sample during the activation process.

Table 3: Mass values before and after the synthesis process for PPAC_WS_N2_1173, PPAC_PEL_N2_1173, PPAC_POW_N2_1173 samples.

Sample name	M_I (g)	M_F (g)	Mass loss (%)	Yield (%)
PPAC_WS_N2_1173	9.72	0.76	92.16	7.84
PPAC_PEL_N2_1173	5.64	0.98	82.66	17.34
PPAC_POW_N2_1173	10.29	1.89	81.64	18.36

3.2.1 Textural characterization

To highlight possible textural differences among the synthetized ACs samples, evaluation of SSA, PSD and VT were obtained by N_2 adsorption/desorption characterization performed at liquid nitrogen temperature up to 1 bar (see Figure 3a and 3b).

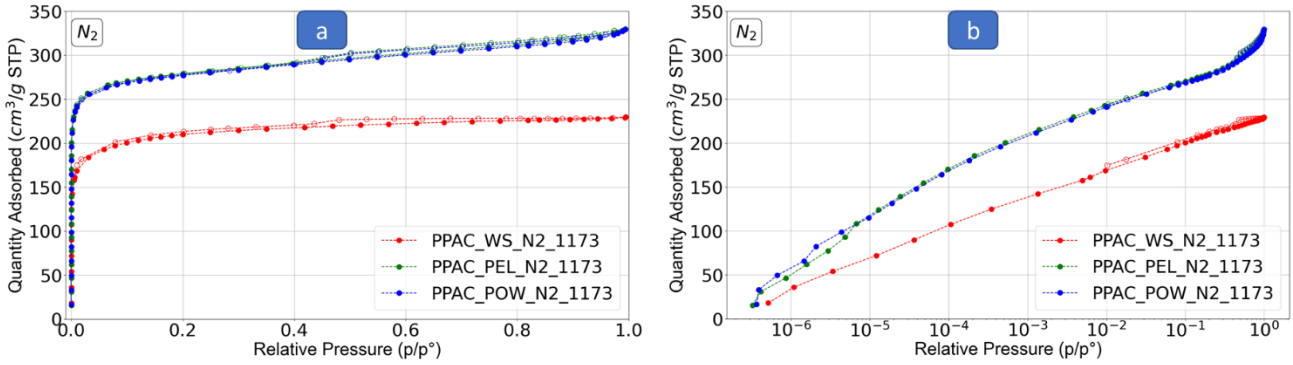

Figure 3: Nitrogen adsorption/desorption isotherms for samples PPAC_WS_N2_1173, PPAC_PEL_N2_1173, PPAC_POW_N2_1173 measured at 77 K: a) linear scale, b) semi-logarithmic scale.

PPAC_WS_N2_1173 sample isotherm shows a trend which, according to the IUPAC classification[49,59,60], can be traced back to a Type I isotherm while PPAC_PEL_N2_1173 and PPAC_POW_N2_1173 samples can be classified as Type I for low pressures values and Type IV for relative pressure higher than 0.3-0.4 P/P_0. A small hysteresis loop [59] is visible for all investigated samples.

The main difference among the three isotherms is related to the quantities of gas adsorbed, in fact, the PPAC_WS_N2_1173 sample is associated to a reduced quantity of adsorbed gas compared to samples PPAC_POW_N2_1173 and PPAC_PEL_N2_1173 (Figure 3a and 3b). As preliminary conclusions can be asserted: 1) PPAC_POW_N2_1173 and PPAC_PEL_N2_1173 samples have higher V_T and SSA than the PPAC_WS_N2_1173; 2) isotherms related to PPAC_POW_N2_1173 and PPAC_PEL_N2_1173 samples are comparable, both in form and Nitrogen capacity, implying that the two samples have comparable textural properties. All the textural properties are summarized in Table 4, while the Pore Size Distribution and the Cumulative Pore Volume are shown in Figure 4.

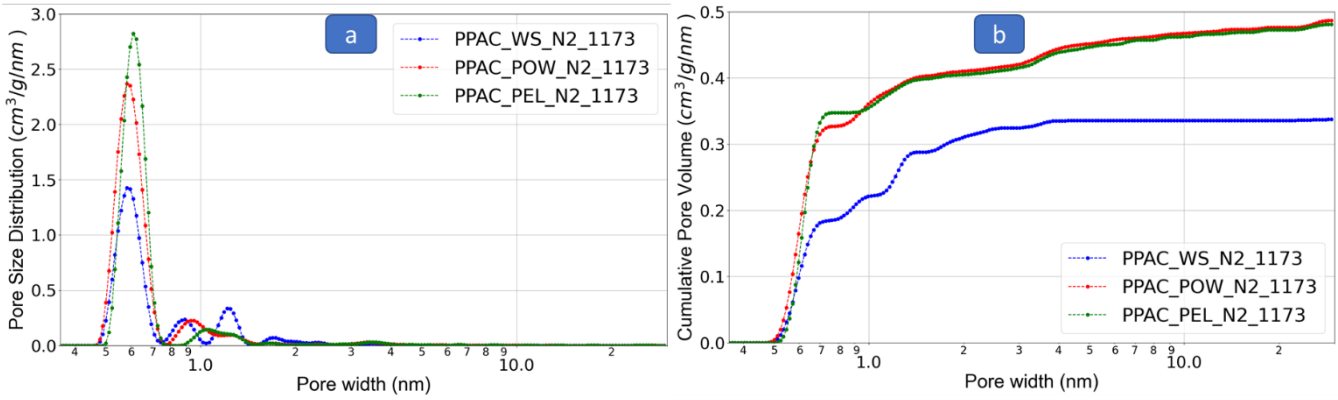

Figure 4: a) Pore size distribution for PPAC_WS_N2_1173, PPAC_PEL__N2_1173, PPAC_POW__N2_1173 samples; b) Cumulative pore volume for PPAC_WS_N2_1173, PPAC_PEL__N2_1173, PPAC_POW__N2_1173 samples;

Table 4: Summary of samples textural properties and SSA derived from the N_2 adsorption isotherms for PPAC_WS_N2_1173, PPAC_PEL_N2_1173, PPAC_POW_N2_1173 samples.

Sample name	V_{ult} ± 0.001 (cm^3/g)	V_{sup} ± 0.001 (cm^3/g)	V_{mic} ± 0.001 (cm^3/g)	V_{mes} ± 0.001 (cm^3/g)	V_T ± 0.001 (cm^3/g)	SSA (m^2/g)
PPAC_WS_N2_1173	0.181	0.127	0.308	0.026	0.334	789.2 ± 2.3
PPAC_PEL_N2_1173	0.333	0.064	0.397	0.076	0.473	1080.4 ± 2.0
PPAC_POW_N2_1173	0.315	0.089	0.404	0.076	0.48	1075.3 ± 2.3

Histograms representing the micro, meso and cumulative pore volumes for analyzed samples (Figure S1a) and a more detailed distinction between ultra-micropores and super-micropores within the micropores volume (Figure S1b) are presented. Looking in detail to the obtained structural characteristics, it is possible to notice that the physical activation process is much more effective for samples PPAC_POW_N2_1173 and PPAC_PEL_N2_1173 rather than for the PPAC_WS_N2_1173 sample.

In fact, the SSA values, obtained for the PPAC_WS_N2_1173 sample is clearly lower than those for samples PPAC_POW_N2_1173 and PPAC_PEL_N2_1173 (see Table 4).

Similarly, analyzing the porous structure of the samples, the total pore volume also turns out to be higher for the PPAC_POW_N2_1173 and PPAC_PEL_N2_1173 samples than for the PPAC_WS_N2_1173. The same trend is reflected also in the volumes associated with ultra-micropores, super-micropores and mesopores that significantly increases (Table 4 and Figures S1a, S1b). This implies that the physicochemical treatment to which the samples were subjected appears to be significantly less effective on whole shells, as regards the development of porosity.

The morphological and chemical characteristics of the samples obtained by SEM and EDX analysis are shown in Figure 5 and Table 5, respectively.

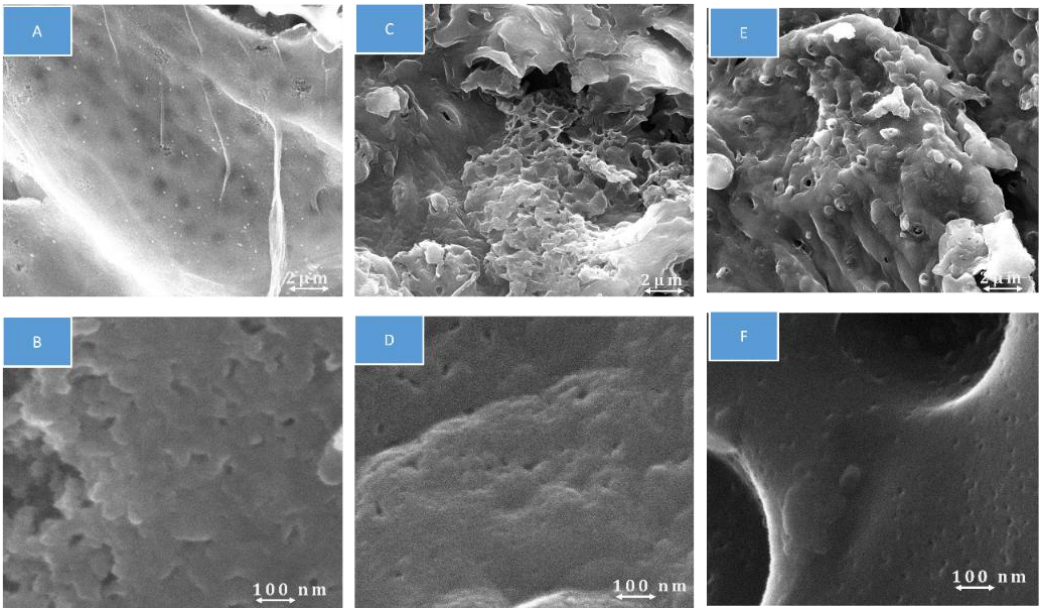

Figure 5: SEM images of samples (A) PPAC_WS_N2_1173 (Scale bar = 2 µm); B) PPAC_WS_N2_1173 (Scale bar = 100 nm); C) PPAC_PEL_N2_1173 (Scale bar = 2 µm; D) PPAC_PEL_N2_1173 (Scale bar = 100 nm; E) PPAC_POW_N2_1173 (Scale bar = 2 µm; F) PPAC_POW_N2_1173 (Scale bar = 100 nm).

The surfaces of the synthesized samples appear very irregular, rough, and highly porous. At higher magnification, macropores and mesopores of variable shape can be observed (Figure 5 B,D,F).

These considerations appear to be in line with what was observed in the XRD analyzes (see Figure S4) in which are not observed well-defined peaks within the spectrums, demonstrating that no long-range crystalline orders are present. The information obtained from the EDX analyzes that the synthetized ACs are amorphous carbon-based materials. This result appears to be in line with what is present in the literature on samples of the same type and subjected to similar synthesis procedure [61].

The chemical composition of the synthesized ACs samples determined by EDX is reported in Table 5, this is the result of several acquisitions carried out in different points of each sample and averaged (see Tables S5-S13).

Table 5: EDX analysis of samples PPAC_WS_N2_1173, PPAC_PEL_N2_1173, PPAC_POW_N2_1173.

	PPAC_WS_N2_1173		PPAC_PEL_N2_1173		PPAC_POW_N2_1173	
Element	**Avg. wt. %**	**Avg. at. %**	**Avg. wt. %**	**Avg. at. %**	**Avg. wt. %**	**Avg. at. %**
C	65.30	73.50	90.90	93.57	95.27	96.87
O	28.73	24.33	7.63	5.87	3.63	2.77
K	5.03	1.73	0.60	0.20	0.77	0.23

By comparing the chemical composition of the untreated precursor (see Table 1) with the synthesized PPAC_WS_N2_1173 sample (see Table 5), one can conclude that the concentrations of carbon, oxygen and potassium are comparable, while the values related to PPAC_PEL_N2_1173 and PPAC_POW_N2_1173 samples appear to be different, with a clear depletion of oxygen with respect to carbon. It is noticeable that the carbonization/activation process is not very effective on the sample deriving from the whole shell, having a chemical composition similar to the one of the precursors (sample not subject to synthesis), while it has a much greater impact on samples deriving from pellets and powder, with much higher concentrations of carbon.

The EDX results are in line with the N_2 adsorption data: 1) PPAC_PEL_N2_1173 and PPAC_POW_N2_1173 samples, have similar TPV, SSA with a similar chemical composition; 2) PPAC_WS_N2_1173 sample, associated with lower TPV and SSA, has a similar chemical to the raw material prior the synthesis.

To study the functional groups, FTIR analysis were performed on all synthetized ACs samples in the range of 850-3780 cm^{-1}. The IR spectra in the ranges of 850-1850 cm^{-1} and 2650-3780 cm^{-1} are shown in Figure 6a,b.

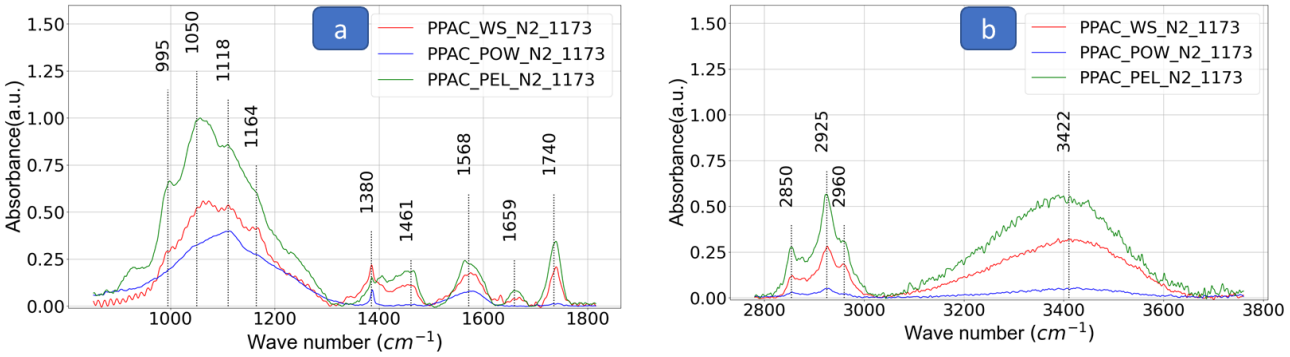

Figure 6: a) FTIR spectra of PPAC_WS_N2_1173, PPAC_POW_N2_1173, PPAC_PEL_N2_1173 samples in the range of 850-1850 cm^{-1};b) : FTIR spectra of samples PPAC_WS_N2_1173, PPAC_POW_N2_1173, PPAC_PEL_N2_1173 in the range of 2650-3780 cm^{-1}.

The peaks relating to the C=O stretching vibrations of carbonyl groups (1740 cm^{-1}), to the C=C stretching (1659 cm^{-1}), to the C-O stretching (1380 cm^{-1}), to the phenol or alcohol vibrations (C-O-C) (respectively 1164 cm^{-1} and 1118 cm^{-1}), and aromatic C-H in-plane deformation (1050 cm^{-1}) are clearly observed in the samples similar to that of the raw material (Figures 1b and 5b). The intensity of the peak at 1740 cm^{-1} is very low for PPAC_POW_N2_1173. This can be attributed to the activating agent-initiated bond cleavage or heat treatment process during production of the ACs [62].

The IR spectra of the raw material (Figures 1 a,b) and of the synthesized ACS representing the O–H stretching vibration of hydroxyl groups (3422 cm^{-1}) and the C–H stretching vibration of

the aliphatic structures (2960, 2925 and 2850 cm^{-1}) are similar. While the aliphaticity of the samples is very sensitive to carbonization and activation processes, leading to a significant decrease in the intensity of asymmetric (2925 cm^{-1}) and symmetric C-H stretching bands (2850 cm^{-1}) [63]. In addition to the peaks present both in the synthesized ACs and in the raw material, after the carbonization/activation processes new peaks appear. In particular (Figure 6a), a band at 1568 cm^{-1} ascribed to C=O stretching vibration of the carbonyl group and C=C stretching vibration of the aromatic rings [64], and a band at 1461 cm^{-1} assigned to C-H bending [65].

3.2.2 Hydrogen adsorption analysis

Comparison of H_2 adsorption/desorption isotherms of samples performed at 77 K, up to 1 bar are depicted in Figure 7.

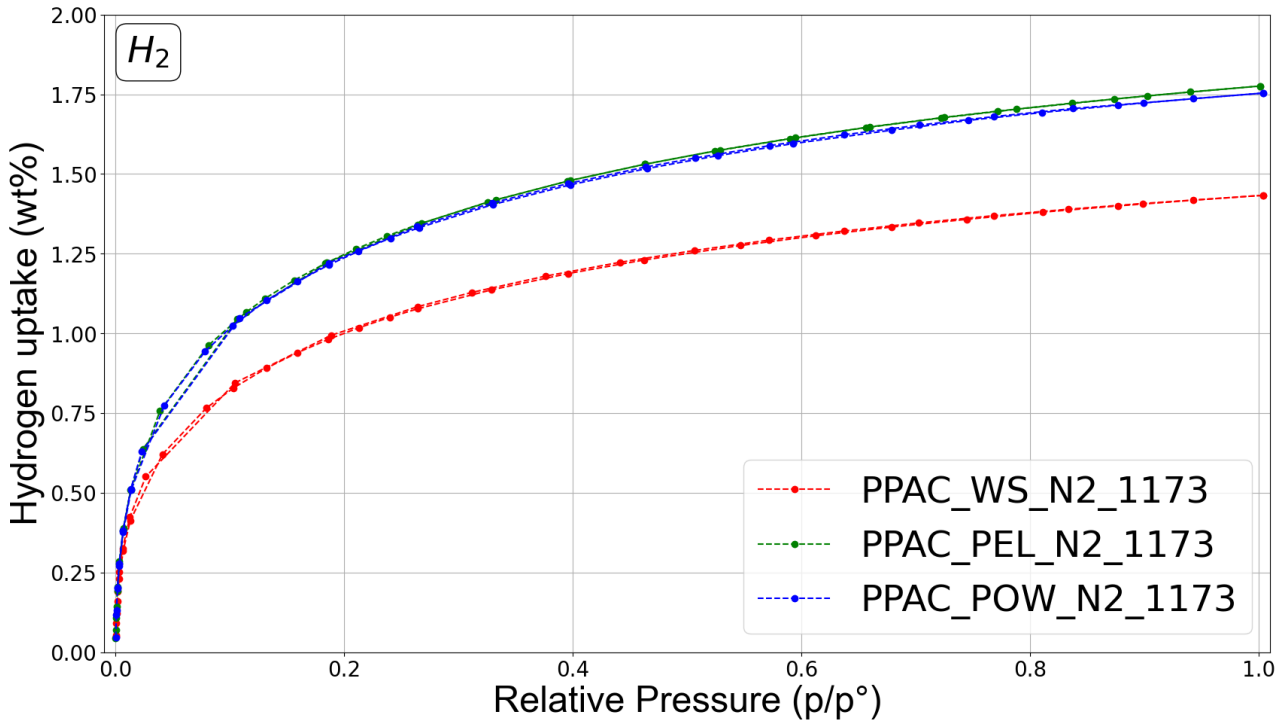

Figure 7: H_2 adsorption/desorption isotherms of samples PPAC_WS_N2_1173, PPAC_POW_N2_1173, PPAC_PEL_N2_1173 samples at 77 K up to 1 bar.

In agreement with the structural and chemical similarities for the samples observed, the textural properties of PPAC_PEL_N2_1173, PPAC_POW_N2_1173 in terms of H_2 adsorption/desorption show similar trend and storage capacity: 1) PPAC_WS_N2_1173 sample shows lower H_2 adsorption; 2) PPAC_POW_N2_1173 and PPAC_PEL_N2_1173 have greater storage capacities as a function of relative pressure being very similar to each other (see Table 6).

Table 6: H2 adsorption capacity of samples PPAC_WS_N2_1173, PPAC_POW_N2_1173, PPAC_PEL_N2_1173 measured at 1 bar H2.

Sample name	Experimental value of wt% at 1 bar ± 0.01
PPAC_WS_N2_1173	1.43
PPAC_PEL_N2_1173	1.77
PPAC_POW_N2_1173	1.75

The determination of the parameters of the Toth model obtained through a fit procedure are summarized in Table S29.

The Toth analysis confirms that at higher pressure (ideally to infinite), the sample with lower performance is the PPAC_WS_N2_1173 while samples PPAC_PEL_N2_1173 and PPAC_POW_N2_1173 have comparable asymptotic and greater adsorption capacity (w_{Max}~ 4.1). It is noteworthy that, all samples show very low and similar value of t parameter (t ~ 0.24) which is in agreement with the high heterogeneity of the samples as observed by SEM and XRD analysis.

For each synthesized sample, the adsorption/desorption isotherms at room temperature up to 1 bar were also acquired (see Figure S3), from which it is possible to observe excellent reversibility of the processes, but low adsorption capacities.

3.3 Optimization of ACs synthesis procedure

After the pre-screening test of the raw material, the next step was optimization of the synthesis procedure towards improving the ACs performance. In particular, PPAC_PEL_N2_1173 sample turns out to be slightly better in terms of H_2 adsorption capacity, slightly higher SSA and ultra-micropore volume than the PPAC_POW_N2_1173. However, the PPAC_PEL_N2_1173 synthesis procedure involves an extra step (palletization). The main change in the synthesis procedure concerns the carbonization process. All previous synthesis had a carbonization process carried out in an inert environment while the activation in an oxidizing environment, but it is known from the literature that the use of CO_2 during the carbonization phase rather than N_2 can favor the formation of porosity, even at temperatures lower than the activation temperature, since CO_2 is more aggressive than N_2 [66]. Additionally, while in the first part of this experimental work all synthesis parameters (such as activation temperature, flow, activation time, etc.) were unchanged and the optimization concerned mainly the type of precursor chosen, in the second part of the present experimental work the precursor was kept fixed, and the activation temperature was changed, since it is known that among the thermodynamic parameters inherent in the synthesis process, the most influential

one is the activation temperature [67]. Starting by choosing an activation temperature of 973 K, this was increased by steps of 100 K. The optimization process required increasing the temperature until a sample with worse performance than the previous one is obtained.

More details on the carbonization and activation process are reported in the supporting information (See tables S16-S17).

In Table 7, the criteria used for naming the samples and the key parameters applied during the pyrolysis are reported.

Table 8 summarizes the mass loss values determined for each synthesis procedure.

Table 7: Samples nomenclature and key pyrolysis parameters. The acronym assigned to the samples uses the information from columns 2, 3, 4 and 5.

Sample name	Raw material	Form	Carbonization Gas	Carbonization range (K)	Activation temperature (K)	Activation Gas	Activation time (min)
PPAC_POW_CO2_973	PPAC (Peach Pit ACs)	POW (Powder)	CO2	673 - 973	973	CO2	60
PPAC_POW_CO2_1073	PPAC (Peach Pit ACs)	POW (Powder)	CO2	673 - 1073	1073		
PPAC_POW_CO2_1173	PPAC (Peach Pit ACs)	POW (Powder)	CO2	673 - 1173	1173		
PPAC_POW_CO2_1273	PPAC (Peach Pit ACs)	POW (Powder)	CO2	673 - 1273	1273		

Table 8: Mass before and after the synthesis process for PPAC_POW_CO2_973, PPAC_POW_CO2_1073, PPAC_POW_CO2_1173, PPAC_POW_CO2_1273 samples.

Sample name	M_I (g)	M_F (g)	Mass loss (%)	Yield (%)
PPAC_ POW_CO2_973	10.33	3.00	71.01	28.99
PPAC_ POW_CO2_1073	10.27	2.38	76.83	23.17
PPAC_ POW_CO2_1173	10.28	1.17	88.66	11.34
PPAC_ POW_CO2_1273	10.31	0.00	100.00	0.00

Considering the PPAC_POW_CO2_1173 sample and the PPAC_POW_N2_1173 sample, these were subjected to the same synthesis process, maintaining the same parameters, simply varying the type of gas considered during the carbonization phase. In this context, a comparison between the two samples allows to understand how the type of gas considered in

the carbonization phase affects the mass loss related to the ACs produced. It is possible to observe that the mass loss related to the PPAC_POW_CO2_1173 sample, i.e. 88.66% (See Table 8), is higher than that of the PPAC_POW_N2_1173 sample, i.e. 82.66% (See Table 3). This evidence appears to be in line with what was determined in the thermogravimetric analyzes (Figures 2a,b), i.e. that CO_2 is more aggressive on the samples than the N_2.

3.3.1 Textural, bulk and surface characterization

By using the volumetric techniques as described in Section 2.1, the SSA, PSD and the V_T of the samples were evaluated. Although four different syntheses were performed, only three samples were analyzed since the final mass of sample PPAC_ POW_CO2_1273 was zero.
The N_2 isotherms of the samples are presented in Figure 8.

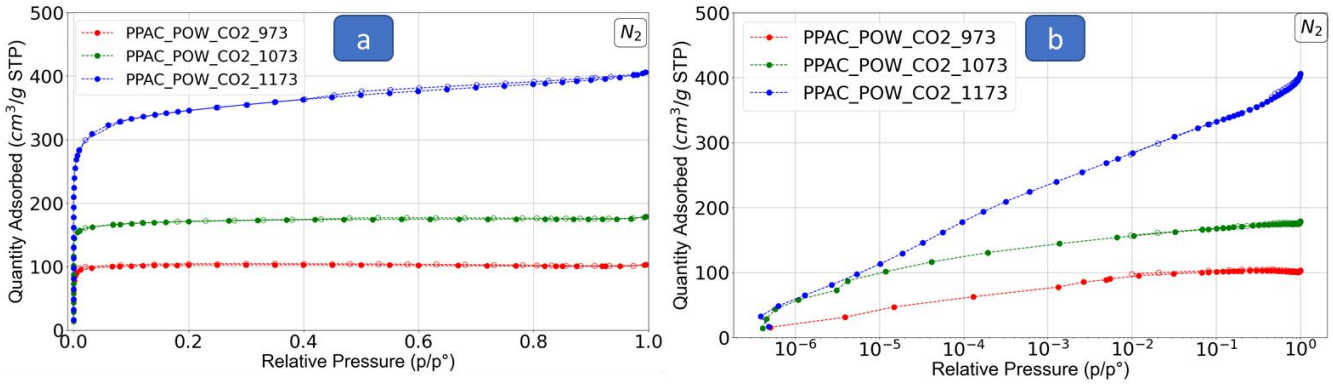

Figure 8: Nitrogen adsorption/desorption isotherms for PPAC_POW_CO2_973, PPAC_POW_CO2_1073, PPAC_POW_CO2_1173 samples measured at 77 K: a) linear scale, b) semi-logarithmic.

The isotherms associated with PPAC_ POW_CO2_973 and PPAC_ POW_CO2_1073 samples, can be identified as Type I(a) according to IUPAC classification. In fact, they exhibit a rapid uptake at low pressures, due to the interactions between the gas and the micropores reaching a plateau at higher pressures [68]. This result provides preliminary information on their PSD indicating variation of pores and a low amount of pores greater than 2 nm [68]. On the other hand, for the PPAC_ POW_CO2_1173 sample, a Type I(b) isotherm represents the rapid uptake at low pressures due to the presence of micropores, but not reaching the plateau at high pressure, indicating a greater presence of mesopores [68].
Figure S2a, S2b show a comparison of micro, meso and cumulative pore volume for all samples, and comparison of ultra, super and micro pores volume, respectively, while in Figure 9a and 9b are reported the total pore volume and cumulative pore volume respectively.

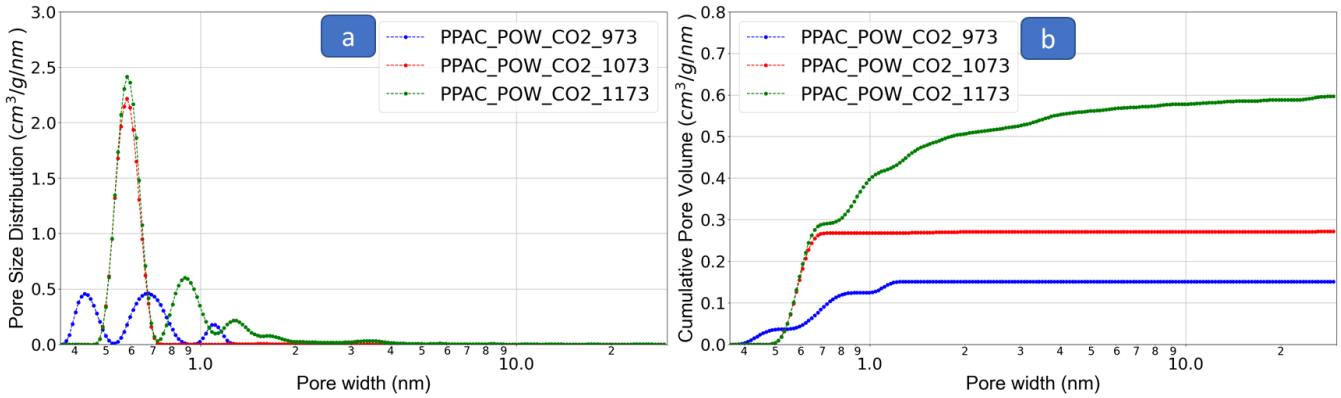

Figure 9: a) Pore size distribution for PPAC_POW_CO2_973, PPAC_POW_CO2_1073, PPAC_POW_CO2_1173 samples; b) Cumulative pore volume for PPAC_POW_CO2_973, PPAC_POW_CO2_1073, PPAC_POW_CO2_1173 samples;

All the structural properties of the samples are summarized in Table 9.

Table 9: Textural properties and SSA derived from the N2 adsorption isotherms for PPAC_POW_CO2_973, PPAC_POW_CO2_1073, PPAC_POW_CO2_1173 samples.

Sample name	**V_{ult} ± 0.001 (cm^3/g)**	**V_{sup} ± 0.001 (cm^3/g)**	**V_{mic} ± 0.001 (cm^3/g)**	**V_{mes} ± 0.001 (cm^3/g)**	**V_T ± 0.001 (cm^3/g)**	**SSA (m^2/g)**
PPAC_POW_CO2_973	0.084	0.061	0.145	-	0.145	335.2 ± 2.2
PPAC_POW_CO2_1073	0.266	0.003	0.269	-	0.269	682.5 ± 1.3
PPAC_POW_CO2_1173	0.288	0.216	0.504	0.089	0.593	1316.8 ± 3.6

The volume related to ultra-micropores increases as the activation temperature increases; the same trend can be observed for total micropores and for the total pore volume. PPAC_POW_CO2_1173 sample has the largest amount of super-micropores, however, the super-micropores volume does not follows the same trend as the ultra-micropores, since PPAC_POW_CO2_973 has a higher volume than the PPAC_POW_CO2_1073. This can be justified by noting that in the PPAC_POW_CO2_1073 sample there is an increase in ultra-micropores, consequently in the PPAC_POW_CO2_1073 sample; the CO_2 is more effective in the formation of ultra-micropores instead of super-micropore.

By further increasing the activation temperature, an increase in ultra-micropores, associated with a rapid increase in super-micropores and mesopores can be noticed, consequently it is possible to state that at 1173 K, CO_2 interacts in a more aggressively way with the surface, creating wider pores, i.e. mesopores, which can favor the formation of super-micropores [69]. Additionally, also the SSA value associated with each sample increases as the activation temperature increases (see Table 9). From structural point of view, it can be concluded that

the best sample is the PPAC_POW_CO2_1173 one since it has higher SSA than the other two, moreover, not only the total pore volume but also the volumes of ultra, super and mesopores are greater.

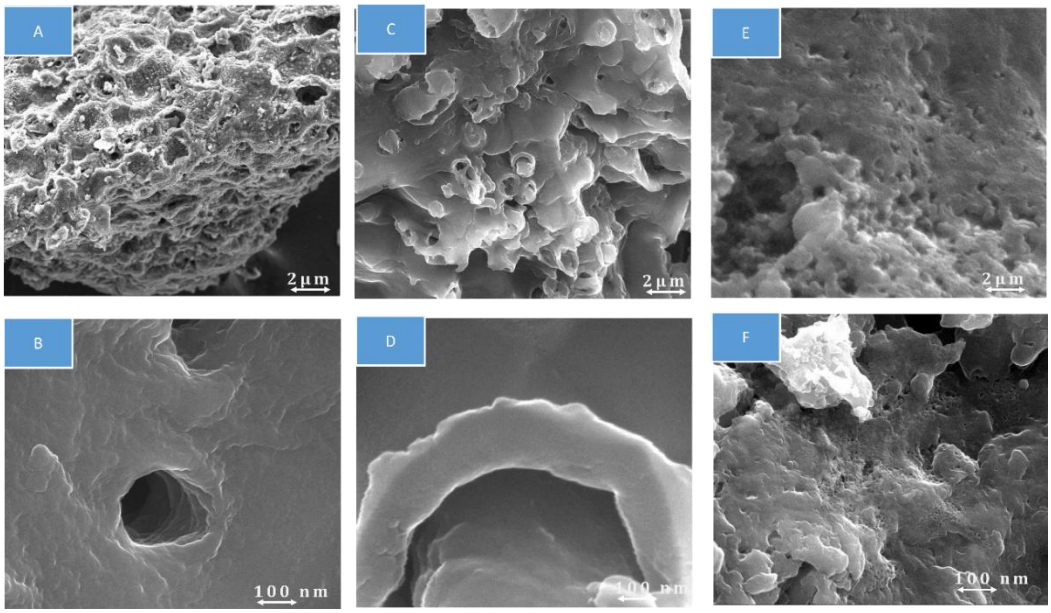

Figure 10: SEM images of sample (A) PPAC_POW_CO2_973 (Scale bar = 2 µm); B) PPAC_POW_CO2_973 (Scale bar = 100 nm; C) (C) PPAC_POW_CO2_1073 (Scale bar = 2 µm); D) PPAC_POW_CO2_1073 (Scale bar = 100 nm); E) PPAC_POW_CO2_1173 (Scale bar = 2 µm; F) PPAC_POW_CO2_1173 (Scale bar = 100 nm).

SEM images of the optimized sample are shown in Figure 10. Highly rough and amorphous surfaces are observed, with no evident order. However, these samples are highly porous, with pores of different shapes and sizes.

What was said in section 3.2.1 regarding EDX analyzes is also valid for these samples. In fact, observing the EDX spectra inherent to the new synthesized ACs (see Figure S5), not even in this case is it possible to distinguish long-range lattice orders.

The chemical composition of the ACs samples is summarized in Table 10 and Tables S20-S28.

Table 10: Chemical composition of samples PPAC_POW_CO2_973, PPAC_POW_CO2_1073, PPAC_POW_CO2_1173 measured by EDX.

	PPAC_ POW_CO2_973		**PPAC_ POW_CO2_1073**		**PPAC_ POW_CO2_1173**	
Element	**Avg. wt. %**	**Avg. at. %**	**Avg. wt. %**	**Avg. at. %**	**Avg. wt. %**	**Avg. at. %**
C	93.63	95.60	96.03	97.37	95.17	96.73
O	5.20	4.00	3.10	2.37	3.87	2.97

K	0.53	0.13	0.57	0.20	0.50	0.17

Both the atomic concentration and the weight of the samples are comparable to each other, and similar to those shown in Table 5 for the PPAC_POW_N2_1173 sample. Based on this observation, one can conclude that the activation temperature, barring small fluctuations, does not substantially change the chemical composition of the samples produced and the type of gas considered during the carbonization phase does not cause significant changes. The FTIR spectra of the samples are shown in Figures 11 a,b .

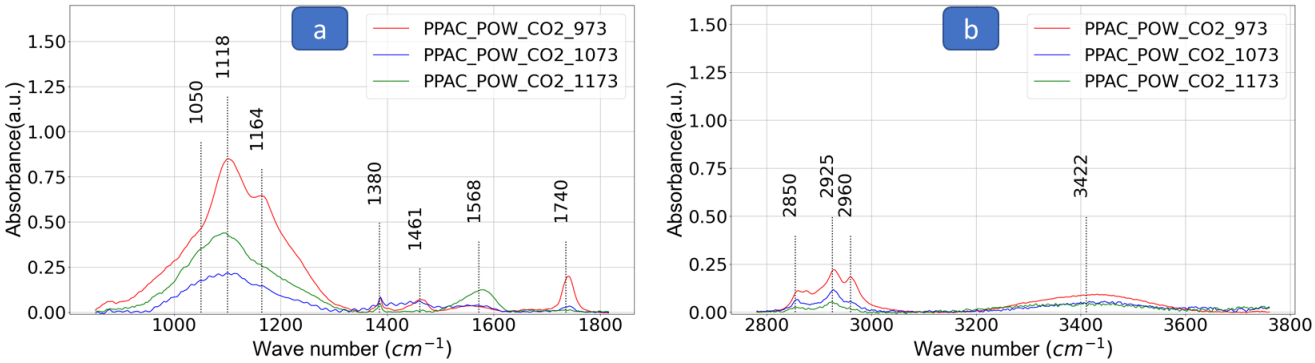

Figure 11: FTIR spectra of samples PPAC_POW_CO2_973, PPAC_POW_CO2_1073, PPAC_POW_CO2_1173 samples in the range of (a) 850-1850 cm^{-1} and (b) 2650-3780 cm^{-1}.

The IR bands observed in the spectra of samples PPAC_WS_N2_1173, PPAC_POW_N2_1173, PPAC_PEL_N2_1173 (Figures 11 a,b) and for the carbonized samples in CO_2 show the same peaks previously observed in Figures 6 a,b . This observation allows to state that the use of CO_2 during the carbonization process rather than N_2, does not lead to the formation of new functional groups which is in line with the EDX analyses.

3.3.2 Hydrogen adsorption analysis

H_2 adsorption results of the samples measured at 77 K up to 1 bar are reported in Figure 12. A well-defined trend of the H_2 adsorption as a function of the activation temperature can be observed. The amount of H_2 absorbed increases as the activation temperature increases. The results are also summarized in Table 11; the maximum experimental adsorption values obtained at the pressure of 1 bar for each sample are reported.

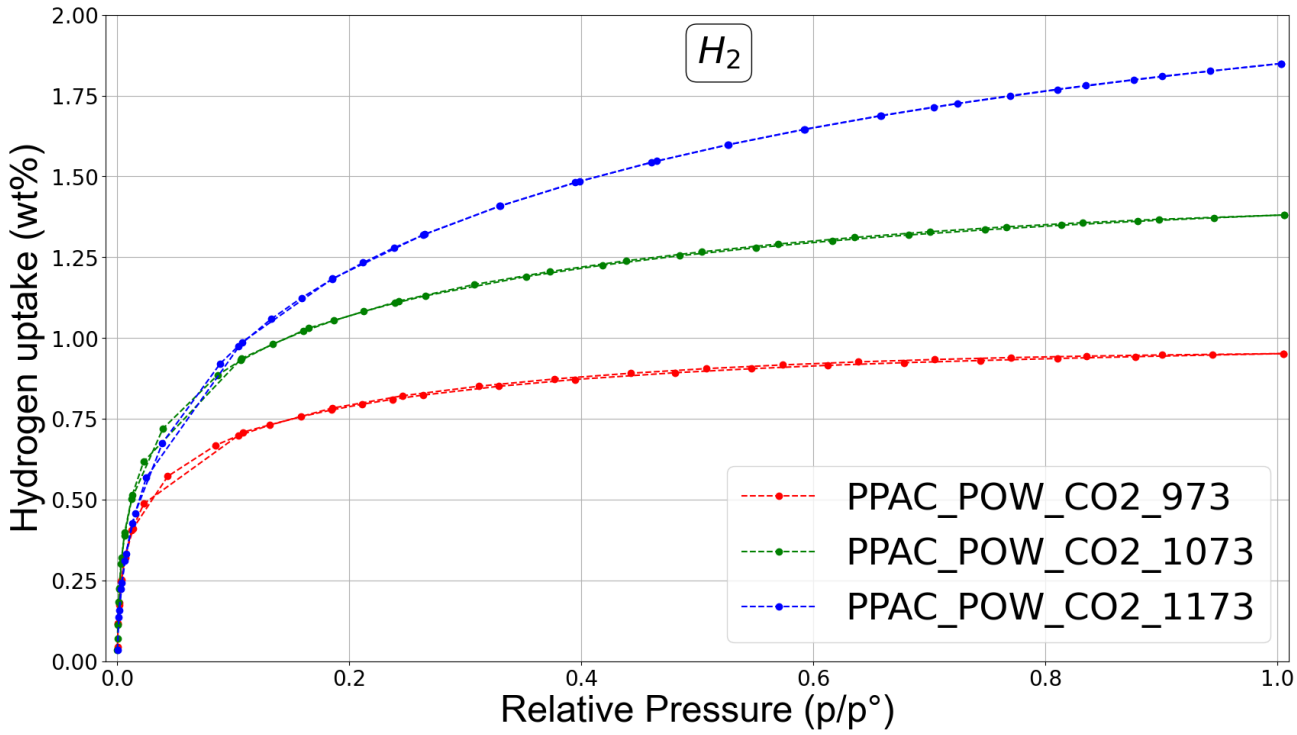

Figure 12: H_2 adsorption isotherms of samples PPAC_POW_CO2_973, PPAC_POW_CO2_1073, PPAC_POW_CO2_1173 measured at 77 K up to 1 bar.

Table 11: Maximum experimental adsorption H2 capacity of samples PPAC_POW_CO2_973, PPAC_POW_CO2_1073, PPAC_POW_CO2_1173 measured at 1 bar.

Sample name	Experimental value of wt% at 1 bar ± 0.01
PPAC_POW_CO2_973	0.95
PPAC_POW_CO2_1073	1.38
PPAC_POW_CO2_1173	1.85

Table S29 shows the values of the three Toth fit parameters obtained for the different samples.

The Toth fit results show that as the activation temperature increases, the value associated with the $wt\%_{MAX}$ increases too, the most performing sample is the PPAC_POW_CO2_1173 which reaches a value of 5.17 $wt\%_{MAX}$ which is far exceeding the values achieved by the other two samples. Moreover, it is noticeable that it decreases as the activation temperature increases. This result can be interpreted as a decrease in surface homogeneity, as a matter of fact that parameter become gradually low reaching t~0.25 at a temperature of 1173 K. Such behavior can be justified by considering that, even the amorphous carbons do not have a long-range surface order, they may have shallow short-range reticular orders [70], consequently, it can be assumed that by increasing the activation temperature, the superficial short-range

orders are also lost. In summary, from both textural and adsorption results one can see that the best sample is PPAC_POW_CO2_1173. It has the highest SSA equal of 1317 m^2/g and of 1.85 wt% H_2 capacity at 1 bar; the experimental results are in a good agreement with the Toth fit, i.e. an asymptotic storage capacity of 5.17 $wt\%_{MAX}$. Following the above conclusions, it is possible to justify why a synthesis was also carried out at 1273 K. Noticing that the adsorption capabilities increase as the activation temperature increases, the process optimization needs to iterate the synthesis procedure, increasing the activation temperature until it reaches 1273 K, and a total degradation of the sample is observed.

Also in this case, H_2 adsorption measurements were acquired at room temperature up to 1 bar and the considerations that can be made are similar to those reported in Section 3.2.2, in fact, as can be seen from Figure S6, the samples show excellent cyclicity, but low adsorption capacity.Once the best sample among those synthesized was determined, i.e. PPAC_POW_CO2_1173, further analyzes were carried out on this to obtain a more complete and detailed characterization.

First of all, the associated isosteric heat of adsorption (ΔH_{ads}) was calculated using the Clausius-Clapeyron relationship (see equation Eq.1)[71], starting from three adsorption isotherms at three different temperatures (77 K, 279.65 K, 285.65 K) up to 1 bar, evaluating the slope of the Arrhenius plot at constant coverage.

$$\Delta H_{ads} = -R\left(\frac{\partial\, ln(P)}{\partial\left(\frac{1}{T}\right)}\right)_{wt.\%} \qquad (1)$$

Since the main goal is to study molecule-surface interactions, it is interesting to focus on low coverages. For this reason, ΔH_{ads} has been evaluated up to a coverage equal to 0.01 wt%.

Figure 13 shows the result of the calculation carried out on the PPAC_POW_CO2_1173 sample, in which an average value of $\Delta H_{ads} = 9.07\ \frac{kJ}{mol}$ is reached. The very low value determined by the analysis implies that the gas-surface interaction that takes place is exclusively physical

adsorption[72].

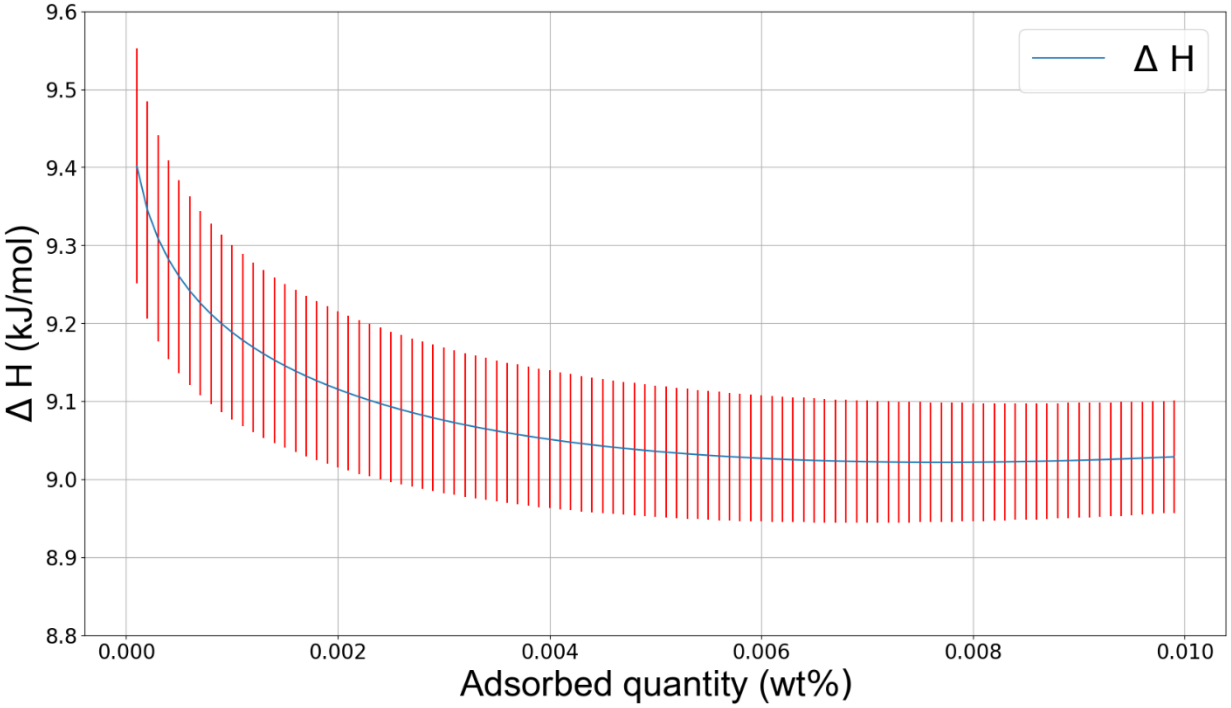

Figure 13: Isosteric heat of adsorption of PPAC_POW_CO2_1173 up to 0.01 wt% derived from three different temperatures (77 K, 279.65 K, 285.65 K) in blue and the related error bar in red.

Secondly, the PPAC_POW_CO2_1173 sample was subjected to high pressure adsorption measurements (up to 80 bar) both at 77 K and at room temperature. Each measurement was repeated three times per day, for two days, for a total of twelve measurements (six at 77 K and six at room temperature), in order to evaluate the cyclicality of the process. After the three measurements of each day, the sample has been degassed at 473 K for 12 hours.

Focusing on the first adsorption/desorption measurement acquired at 77 K up to 80 bar (see Figure 14 a), it is possible to observe excellent storage capacities even at high pressures, reaching a value of 3.45 $wt\%$, and an extremely reduced hysteresis.

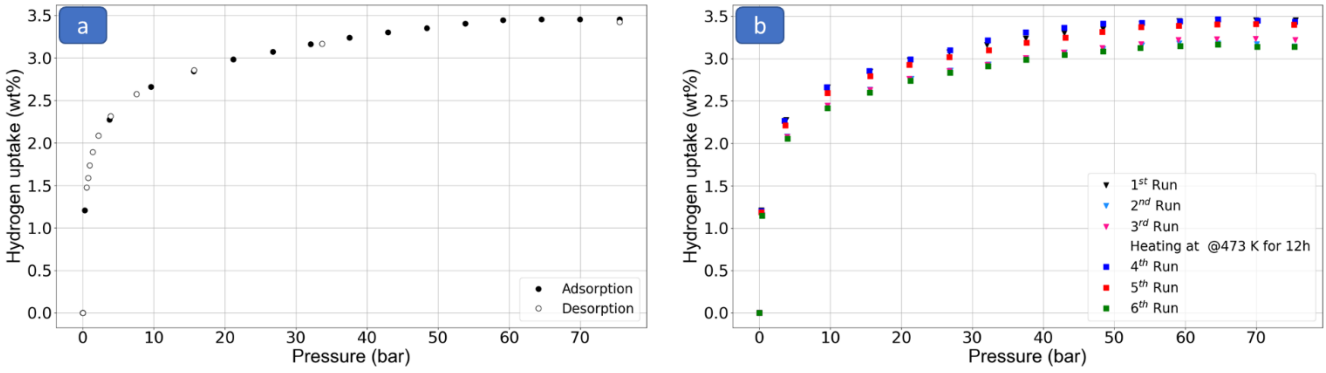

Figure 14: a) First adsorption/desorption measurement up to 80 bar at 77 K on PPAC_POW_CO2_1173 sample; b) All six adsorption measurement up to 80 bar at 77 K on PPAC_POW_CO2_1173 sample. The triangles refer to the measurements taken on the first day, while the squares refer to the measurements taken on the second day.

Analyzing all the adsorption measurements acquired at 77 K (see Figure 14 b), it is possible to observe high reversibility of the processes, in fact, even if H_2 maximum storage capacity is

reached in the first measurement of each day (3.45 wt% at 80 bar), this reduction in the other measurements is relatively small (the third of the first day reaches a value of 3.14 wt% at 80 bar). This evidence is observed for both days of measurement.

In addition to what has been said so far on the cyclical nature of the process, it is also possible to note from Figure 14b that the degassing process, which occurs between the first three measurements and the second three, restore the sample to its initial condition, allowing it to adsorb in the fourth measure the same quantity of gas as the first measurement.

The same analysis was then done on the measurements acquired up to 80 bar at room temperature.

Figure 15a shows the first adsorption/desorption isotherm acquired up to 80 bar at Room Temperature. This has a low storage capacity at room temperature (0.28 wt% at 80 bar), but a very low hysteresis, indicating excellent reversibility of the process.

Figure 15b compares the six adsorption isotherms acquired for the PPAC_POW_CO2_1173 sample during the two days of analysis up to 80 bar at room temperature. Also in this case, it is possible to observe excellent cyclicity in the adsorption processes, since that the isotherms acquired during the various measurements are very similar to each other.

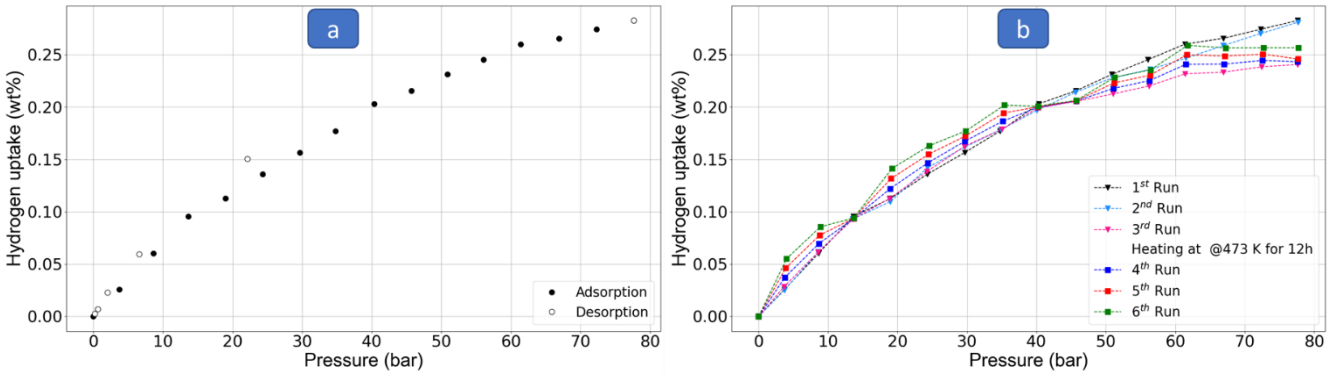

Figure 15: a) First adsorption/desorption measurement up to 80 bar at room temperature K on PPAC_POW_CO2_1173 sample; b) All six adsorption measurement up to 80 bar at room temperature K on PPAC_POW_CO2_1173 sample. The triangles refer to the measurements taken on the first day, while the squares refer to the measurements taken on the second day.

4. Conclusion

In this study, the influence of different raw materials on porosity formation and precursor selection for ACs was investigated. Three samples were synthesized using peach pit whole shells, powdered, and pelletized forms. Among them, the powdered precursor (PPAC_POW_N2_1173) showed the best structural characteristics and H_2 adsorption performance. Building upon these initial results, the synthesis process was further optimized to enhance porosity and H_2 adsorption capacity. By replacing the inert (N_2) carbonization atmosphere with an oxidizing (CO_2) atmosphere and varying the activation temperature, significant improvements were achieved in the textural properties (SSA and VT) by 22.5% and 23.5%, respectively. The best activation temperature was determined to be 1173 K, resulting in the PPAC_POW_CO2_1173 sample with a high H_2 adsorption capacity of 1.85 wt% at 1 bar and 77 K and a surface area of approximately 1316.8 m^2/g, but not excellent storage

capacity up to 1 bar at room temperature. This material exhibited a highly microporous structure, with associated volumes superior to the previously synthesized samples. The EDX analysis confirmed a higher carbon content with increasing temperature and a low presence of oxygen and XRD measurements confirmed the amorphous nature of the treated materials.

FTIR analysis revealed the formation of new surface functional groups during the carbonization/activation process that were not present in the raw material. Importantly, gas variations during carbonization did not lead to the formation of new surface functional groups.

The optimization of the ACs synthesis process successfully produced a nanoporous structure with pores diameter < 2 nm, significantly improving H_2 adsorption capacity.

By comparing the structural properties (SSA and TPV) and the H_2 adsorption uptake at 77 K up to 1 bar (wt%) of the best of the synthesized samples, i.e. PPAC_POW_CO2_1173, with similar materials (carbon-based materials subjected to physical activation) present in the literature, it is possible to note that PPAC_POW_CO2_1173 sample presents comparable values of SSA and TPV, if not higher, moreover it shows excellent performances also in terms of H_2 storage capacity. A comparison between PPAC_POW_CO2_1173 sample and similar ACs reported in the literature is reported in Table S30.

Further high pressure analysis, up to 80 bar at 77 K on the PPAC_POW_CO2_1173 sample, showed good H_2 storage capabilities reaching a value of 3.45 $wt\%$. By repeating the measurements several times, an excellent cyclicity of the sample in the adsorption processes was also observed. Cyclicality also observed in the measurements carried out at room temperature, although with reduced storage capacities.

In conclusion, this research has shed light on the importance of precursor selection, carbonization atmosphere, and activation temperature in tailoring the structural and adsorption properties of activated carbons. The findings contribute to the development of advanced materials with potential applications in H_2 storage and other related fields. Thus, the synthesized ACs exhibit interesting storage properties, making them promising materials for the development of environmentally sustainable materials. In particular, the great value of these materials lies in the type of precursors selected, which from a circular economy perspective, allows the recovery of waste materials, transforming them in a new possible resource, capable of being exploited in different application fields in the coming years.

Supporting information

Supporting Information contains a series of tables and figures that adds further information at the experimental analysis and procedure.

- Tables:
  - S1-S13, S20-S28 refer to the individual EDX analyzes;
  - S14, S16-S19 refer to the synthesis parameters used in the synthesis;

- S15, S29 refer to the parameters obtained from the Toth fit;
- S30 compares different ACs properties present in the literature;

- Figures:
  - S1and S2 refers to the histograms of pore volume;
  - S3, S6 represent the adsorption/desorption isotherms at room temperature up to 1 bar;
  - S4 and S5 refers to the XRD analysis;
  - S7 refers sample before (Peach pit) and after (ACs) treatment.

Acknowledgement

This research was supported by the National Recovery and Resilience Plan (PNRR), funded by the Italian Ministry of the Environment and Energy Security, project "Novel Materials for Hydrogen storage (NoMaH)", ID RSH2A_000035, CUP: F27G22000180006.

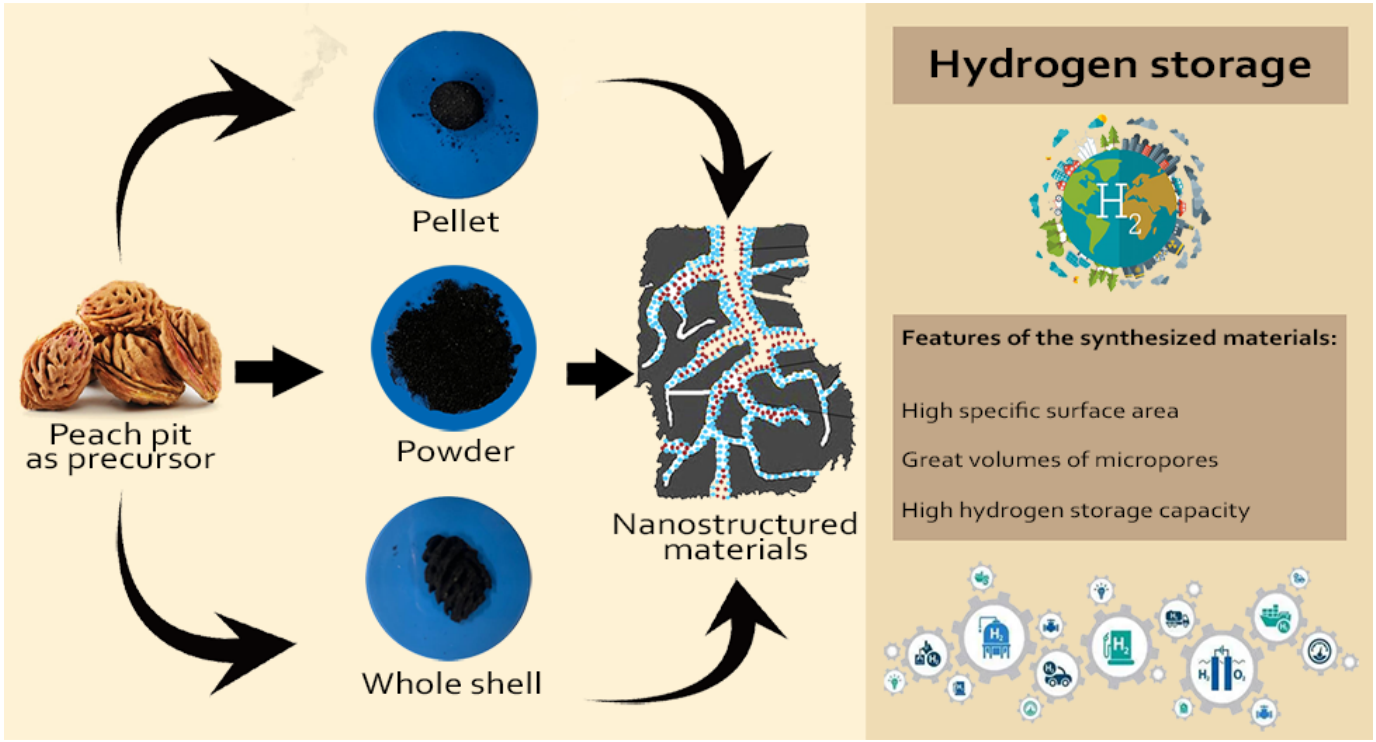
Peach pit
as precursor
Pellet
Powder
Whole shell
Nanostructured
materials
Hydrogen storage
Features of the synthesized materials:
High specific surface area
Great volumes of micropores
High hydrogen storage capacity

Bibliography

(1) Chapman, L. Transport and Climate Change: A Review. *Journal of Transport Geography* **2007**, *15* (5), 354–367. https://doi.org/10.1016/j.jtrangeo.2006.11.008.

(2) Kessel, D. G. Global Warming — Facts, Assessment, Countermeasures. *Journal of Petroleum Science and Engineering* **2000**, *26* (1–4), 157–168. https://doi.org/10.1016/S0920-4105(00)00030-9.

(3) Yue, M.; Lambert, H.; Pahon, E.; Roche, R.; Jemei, S.; Hissel, D. Hydrogen Energy Systems: A Critical Review of Technologies, Applications, Trends and Challenges. *Renewable and Sustainable Energy Reviews* **2021**, *146*, 111180. https://doi.org/10.1016/j.rser.2021.111180.

(4) Pan, A.; Liu, J.; Liu, Z.; Yang, Y.; Yang, X.; Zhang, M. Application of Hydrogen Energy and Review of Current Conditions. *IOP Conf. Ser.: Earth Environ. Sci.* **2020**, *526* (1), 012124. https://doi.org/10.1088/1755-1315/526/1/012124.

(5) Luberti, M.; Ahn, H. Review of Polybed Pressure Swing Adsorption for Hydrogen Purification. *International Journal of Hydrogen Energy* **2022**, *47* (20), 10911–10933. https://doi.org/10.1016/j.ijhydene.2022.01.147.

(6) Nordell, B. Thermal Pollution Causes Global Warming. *Global and Planetary Change* **2003**, *38* (3–4), 305–312. https://doi.org/10.1016/S0921-8181(03)00113-9.

(7) Jacobson, M. Z. *Air Pollution and Global Warming: History, Science, and Solutions*, 2nd ed.; Cambridge University Press, 2012. https://doi.org/10.1017/CBO9781139109444.

(8) Herndon, J. M.; Whiteside, M. Further Evidence That Particulate Pollution Is the Principal Cause of Global Warming: Humanitarian Considerations. *JGEESI* **2019**, 1–11. https://doi.org/10.9734/jgeesi/2019/v21i130117.

(9) LINDSEY, R. Climate Change: Global Sea Level. **2022**.

(10) Perera, F.; Nadeau, K. Climate Change, Fossil-Fuel Pollution, and Children's Health. *N Engl J Med* **2022**, *386* (24), 2303–2314. https://doi.org/10.1056/NEJMra2117706.

(11) Costello, A.; Abbas, M.; Allen, A.; Ball, S.; Bell, S.; Bellamy, R.; Friel, S.; Groce, N.; Johnson, A.; Kett, M.; Lee, M.; Levy, C.; Maslin, M.; McCoy, D.; McGuire, B.; Montgomery, H.; Napier, D.; Pagel, C.; Patel, J.; De Oliveira, J. A. P.; Redclift, N.; Rees, H.; Rogger, D.; Scott, J.; Stephenson, J.; Twigg, J.; Wolff, J.; Patterson, C. Managing the Health Effects of Climate Change. *The Lancet* **2009**, *373* (9676), 1693–1733. https://doi.org/10.1016/S0140-6736(09)60935-1.

(12) Denchak, M. Are the Effects of Global Warming Really That Bad? **2022**.

(13) Thomas, K. M. Hydrogen Adsorption and Storage on Porous Materials☆. *Catalysis Today* **2007**, *120* (3–4), 389–398. https://doi.org/10.1016/j.cattod.2006.09.015.

(14) Zhao, X. B.; Xiao, B.; Fletcher, A. J.; Thomas, K. M. Hydrogen Adsorption on Functionalized Nanoporous Activated Carbons. *J. Phys. Chem. B* **2005**, *109* (18), 8880–8888. https://doi.org/10.1021/jp050080z.

(15) Klemeš, J. J.; Varbanov, P. S.; Walmsley, T. G.; Foley, A. Process Integration and Circular Economy for Renewable and Sustainable Energy Systems. *Renewable and Sustainable Energy Reviews* **2019**, *116*, 109435. https://doi.org/10.1016/j.rser.2019.109435.

(16) Kopac, T.; Toprak, A. Hydrogen Sorption Characteristics of Zonguldak Region Coal Activated by Physical and Chemical Methods. *Korean J. Chem. Eng.* **2009**, *26* (6), 1700–1705. https://doi.org/10.1007/s11814-009-0250-3.

(17) Jin, H.; Lee, Y. S.; Hong, I. Hydrogen Adsorption Characteristics of Activated Carbon. *Catalysis Today* **2007**, *120* (3–4), 399–406. https://doi.org/10.1016/j.cattod.2006.09.012.

(18) Nazir, G.; Rehman, A.; Hussain, S.; Aftab, S.; Heo, K.; Ikram, M.; Patil, S. A.; Aizaz Ud Din, M. Recent Advances and Reliable Assessment of Solid-State Materials for Hydrogen Storage: A Step Forward toward a Sustainable H_2 Economy. *Advanced Sustainable Systems* **2022**, *6* (11), 2200276. https://doi.org/10.1002/adsu.202200276.

(19) Abdin, Z.; Zafaranloo, A.; Rafiee, A.; Mérida, W.; Lipiński, W.; Khalilpour, K. R. Hydrogen as an Energy Vector. *Renewable and Sustainable Energy Reviews* **2020**, *120*, 109620. https://doi.org/10.1016/j.rser.2019.109620.

(20) Rehman, A.; Nazir, G.; Heo, K.; Hussain, S.; Ikram, M.; Mahmood, Q.; Alshahrani, T.; Abd-Rabboh, H. S. M. Single Step Strategy to Prepare Highly Microporous Carbons Derived from Melamine and Terephthalaldehyde for High-Performance Material-Based Hydrogen Storage. *Journal of Energy Storage* **2023**, *66*, 107468. https://doi.org/10.1016/j.est.2023.107468.

(21) Crowl, D. A.; Jo, Y.-D. The Hazards and Risks of Hydrogen. *Journal of Loss Prevention in the Process Industries* **2007**, *20* (2), 158–164. https://doi.org/10.1016/j.jlp.2007.02.002.

(22) Férey, G. Hybrid Porous Solids: Past, Present, Future. *Chem. Soc. Rev.* **2008**, *37* (1), 191–214. https://doi.org/10.1039/B618320B.

(23) Iglauer, S.; Abid, H.; Al-Yaseri, A.; Keshavarz, A. Hydrogen Adsorption on Sub-Bituminous Coal: Implications for Hydrogen Geo-Storage. *Geophysical Research Letters* **2021**, *48* (10). https://doi.org/10.1029/2021GL092976.

(24) Abánades, A. Perspectives on Hydrogen. *Energies* **2022**, *16* (1), 437. https://doi.org/10.3390/en16010437.
(25) Jawhari, A. H. Novel Nanomaterials for Hydrogen Production and Storage: Evaluating the Futurity of Graphene/Graphene Composites in Hydrogen Energy. *Energies* **2022**, *15* (23), 9085. https://doi.org/10.3390/en15239085.
(26) Ho, T. M.; Howes, T.; Bhandari, B. R. Encapsulation of Gases in Powder Solid Matrices and Their Applications: A Review. *Powder Technology* **2014**, *259*, 87–108. https://doi.org/10.1016/j.powtec.2014.03.054.
(27) Kopac, T. Hydrogen Storage Characteristics of Bio-based Porous Carbons of Different Origin: A Comparative Review. *Intl J of Energy Research* **2021**, *45* (15), 20497–20523. https://doi.org/10.1002/er.7130.
(28) Ding, Y.; Qi, J.; Hou, R.; Liu, B.; Yao, S.; Lang, J.; Chen, J.; Yang, B. Preparation of High-Performance Hierarchical Porous Activated Carbon via a Multistep Physical Activation Method for Supercapacitors. *Energy Fuels* **2022**, *36* (10), 5456–5464. https://doi.org/10.1021/acs.energyfuels.2c00688.
(29) Yuan, X.; Kumar, N. M.; Brigljević, B.; Li, S.; Deng, S.; Byun, M.; Lee, B.; Lin, C. S. K.; Tsang, D. C. W.; Lee, K. B.; Chopra, S. S.; Lim, H.; Ok, Y. S. Sustainability-Inspired Upcycling of Waste Polyethylene Terephthalate Plastic into Porous Carbon for CO_2 Capture. *Green Chem.* **2022**, *24* (4), 1494–1504. https://doi.org/10.1039/D1GC03600A.
(30) Yin, Y.; Liu, Q.; Wang, J.; Zhao, Y. Recent Insights in Synthesis and Energy Storage Applications of Porous Carbon Derived from Biomass Waste: A Review. *International Journal of Hydrogen Energy* **2022**, *47* (93), 39338–39363. https://doi.org/10.1016/j.ijhydene.2022.09.121.
(31) Rudke, C. R. M.; Zielinski, A. A. F.; Ferreira, S. R. S. From Biorefinery to Food Product Design: Peach (Prunus Persica) By-Products Deserve Attention. *Food Bioprocess Technol* **2023**, *16* (6), 1197–1215. https://doi.org/10.1007/s11947-022-02951-9.
(32) Dias, J. M.; Alvim-Ferraz, M. C. M.; Almeida, M. F.; Rivera-Utrilla, J.; Sánchez-Polo, M. Waste Materials for Activated Carbon Preparation and Its Use in Aqueous-Phase Treatment: A Review. *Journal of Environmental Management* **2007**, *85* (4), 833–846. https://doi.org/10.1016/j.jenvman.2007.07.031.
(33) Lafi, W. K. Production of Activated Carbon from Acorns and Olive Seeds. *Biomass and Bioenergy* **2001**, *20* (1), 57–62. https://doi.org/10.1016/S0961-9534(00)00062-3.
(34) Lussier, M. G.; Shull, J. C.; Miller, D. J. Activated Carbon from Cherry Stones. *Carbon* **1994**, *32* (8), 1493–1498. https://doi.org/10.1016/0008-6223(94)90144-9.
(35) Vilén, A.; Laurell, P.; Vahala, R. Comparative Life Cycle Assessment of Activated Carbon Production from Various Raw Materials. *Journal of Environmental Management* **2022**, *324*, 116356. https://doi.org/10.1016/j.jenvman.2022.116356.
(36) De Rose, E.; Bartucci, S.; Poselle Bonaventura, C.; Conte, G.; Agostino, R. G.; Policicchio, A. Effects of Activation Temperature and Time on Porosity Features of Activated Carbons Derived from Lemon Peel and Preliminary Hydrogen Adsorption Tests. *Colloids and Surfaces A: Physicochemical and Engineering Aspects* **2023**, *672*, 131727. https://doi.org/10.1016/j.colsurfa.2023.131727.
(37) Nazir, G.; Rehman, A.; Hussain, S.; Afzal, A. M.; Dastgeer, G.; Rehman, M. A.; Akhter, Z.; Al-Muhimeed, T. I.; AlObaid, A. A. Heteroatoms-Doped Hierarchical Porous Carbons: Multifunctional Materials for Effective Methylene Blue Removal and Cryogenic Hydrogen Storage. *Colloids and Surfaces A: Physicochemical and Engineering Aspects* **2021**, *630*, 127554. https://doi.org/10.1016/j.colsurfa.2021.127554.
(38) Lewoyehu, M. Comprehensive Review on Synthesis and Application of Activated Carbon from Agricultural Residues for the Remediation of Venomous Pollutants in Wastewater. *Journal of Analytical and Applied Pyrolysis* **2021**, *159*, 105279. https://doi.org/10.1016/j.jaap.2021.105279.
(39) Conte, G.; Stelitano, S.; Policicchio, A.; Minuto, F. D.; Lazzaroli, V.; Galiano, F.; Agostino, R. G. Assessment of Activated Carbon Fibers from Commercial Kevlar® as Nanostructured Material for Gas Storage: Effect of Activation Procedure and Adsorption of CO2 and CH4. *Journal of Analytical and Applied Pyrolysis* **2020**, *152*, 104974. https://doi.org/10.1016/j.jaap.2020.104974.
(40) Tomoda, B. T.; Yassue-Cordeiro, P. H.; Ernesto, J. V.; Lopes, P. S.; Péres, L. O.; Da Silva, C. F.; De Moraes, M. A. Characterization of Biopolymer Membranes and Films: Physicochemical, Mechanical, Barrier, and Biological Properties. In *Biopolymer Membranes and Films*; Elsevier, 2020; pp 67–95. https://doi.org/10.1016/B978-0-12-818134-8.00003-1.
(41) Abu Bakar, M. S.; Ahmed, A.; Jeffery, D. M.; Hidayat, S.; Sukri, R. S.; Mahlia, T. M. I.; Jamil, F.; Khurrum, M. S.; Inayat, A.; Moogi, S.; Park, Y.-K. Pyrolysis of Solid Waste Residues from Lemon Myrtle Essential Oils Extraction for Bio-Oil Production. *Bioresource Technology* **2020**, *318*, 123913. https://doi.org/10.1016/j.biortech.2020.123913.
(42) Salgado, M. D. F.; Abioye, A. M.; Junoh, M. M.; Santos, J. A. P.; Ani, F. N. Preparation of Activated Carbon from Babassu Endocarpunder Microwave Radiation by Physical Activation. *IOP Conf. Ser.: Earth Environ. Sci.* **2018**, *105*, 012116. https://doi.org/10.1088/1755-1315/105/1/012116.

(43) Vernon-Parry, K. D. Scanning Electron Microscopy: An Introduction. *III-Vs Review* **2000**, *13* (4), 40–44. https://doi.org/10.1016/S0961-1290(00)80006-X.
(44) Srivastava, A.; Jain, V. K.; Srivastava, A. SEM-EDX Analysis of Various Sizes Aerosols in Delhi India. *Environ Monit Assess* **2009**, *150* (1–4), 405–416. https://doi.org/10.1007/s10661-008-0239-0.
(45) Hellmann, L.; Schmitz, A. P. D. O.; Módenes, A. N.; Hinterholz, C. L.; Antoniolli, C. D. A. PEACH PIT CHEMICALLY TREATED BIOMASS AS A BIOSORBENT FOR METFORMIN HYDROCHLORIDE REMOVAL: MODELING AND SORPTION MECHANISMS. *Eng. Agríc.* **2021**, *41* (2), 181–195. https://doi.org/10.1590/1809-4430-eng.agric.v41n2p181-195/2021.
(46) Policicchio, A.; Maccallini, E.; Kalantzopoulos, G. N.; Cataldi, U.; Abate, S.; Desiderio, G.; Agostino, R. G. Volumetric Apparatus for Hydrogen Adsorption and Diffusion Measurements: Sources of Systematic Error and Impact of Their Experimental Resolutions. *Review of Scientific Instruments* **2013**, *84* (10), 103907. https://doi.org/10.1063/1.4824485.
(47) Van Erp, T. S.; Martens, J. A. A Standardization for BET Fitting of Adsorption Isotherms. *Microporous and Mesoporous Materials* **2011**, *145* (1–3), 188–193. https://doi.org/10.1016/j.micromeso.2011.05.022.
(48) Kurth, S.; Marques, M. A. L.; Gross, E. K. U. Density-Functional Theory. In *Encyclopedia of Condensed Matter Physics*; Elsevier, 2005; pp 395–402. https://doi.org/10.1016/B0-12-369401-9/00445-9.
(49) Thommes, M.; Kaneko, K.; Neimark, A. V.; Olivier, J. P.; Rodriguez-Reinoso, F.; Rouquerol, J.; Sing, K. S. W. Physisorption of Gases, with Special Reference to the Evaluation of Surface Area and Pore Size Distribution (IUPAC Technical Report). *Pure and Applied Chemistry* **2015**, *87* (9–10), 1051–1069. https://doi.org/10.1515/pac-2014-1117.
(50) Occelli, M. L.; Olivier, J. P.; Perdigon-Melon, J. A.; Auroux, A. Surface Area, Pore Volume Distribution, and Acidity in Mesoporous Expanded Clay Catalysts from Hybrid Density Functional Theory (DFT) and Adsorption Microcalorimetry Methods. *Langmuir* **2002**, *18* (25), 9816–9823. https://doi.org/10.1021/la020567o.
(51) Kowalczyk, P.; Terzyk, A. P.; Gauden, P. A.; Leboda, R.; Szmechtig-Gauden, E.; Rychlicki, G.; Ryu, Z.; Rong, H. Estimation of the Pore-Size Distribution Function from the Nitrogen Adsorption Isotherm. Comparison of Density Functional Theory and the Method of Do and Co-Workers. *Carbon* **2003**, *41* (6), 1113–1125. https://doi.org/10.1016/S0008-6223(03)00019-8.
(52) Zdravkov, B.; Čermák, J.; Šefara, M.; Janků, J. Pore Classification in the Characterization of Porous Materials: A Perspective. *Open Chemistry* **2007**, *5* (2), 385–395. https://doi.org/10.2478/s11532-007-0017-9.
(53) Tóth, J. Uniform Interpretation of Gas/Solid Adsorption. *Advances in Colloid and Interface Science* **1995**, *55*, 1–239. https://doi.org/10.1016/0001-8686(94)00226-3.
(54) Romanos, J.; Beckner, M.; Stalla, D.; Tekeei, A.; Suppes, G.; Jalisatgi, S.; Lee, M.; Hawthorne, F.; Robertson, J. D.; Firlej, L.; Kuchta, B.; Wexler, C.; Yu, P.; Pfeifer, P. Infrared Study of Boron–Carbon Chemical Bonds in Boron-Doped Activated Carbon. *Carbon* **2013**, *54*, 208–214. https://doi.org/10.1016/j.carbon.2012.11.031.
(55) Bathini, V.; Kalakandan, S. K.; Pakkirisamy, M.; Ravichandran, K. Structural Elucidation of Peanut, Sunflower and Gingelly Oils by Using FTIR and 1H NMR Spectroscopy. *PJ* **2018**, *10* (4), 753–757. https://doi.org/10.5530/pj.2018.4.126.
(56) Yang, T.; Lua, A. C. Characteristics of Activated Carbons Prepared from Pistachio-Nut Shells by Physical Activation. *Journal of Colloid and Interface Science* **2003**, *267* (2), 408–417. https://doi.org/10.1016/S0021-9797(03)00689-1.
(57) Shin, S.; Jang, J.; Yoon, S.-H.; Mochida, I. A Study on the Effect of Heat Treatment on Functional Groups of Pitch Based Activated Carbon Fiber Using FTIR. *Carbon* **1997**, *35* (12), 1739–1743. https://doi.org/10.1016/S0008-6223(97)00132-2.
(58) Wibawa, P. J.; Nur, M.; Asy'ari, M.; Nur, H. SEM, XRD and FTIR Analyses of Both Ultrasonic and Heat Generated Activated Carbon Black Microstructures. *Heliyon* **2020**, *6* (3), e03546. https://doi.org/10.1016/j.heliyon.2020.e03546.
(59) Rahman, Md. M.; Shafiullah, A. Z.; Pal, A.; Islam, Md. A.; Jahan, I.; Saha, B. B. Study on Optimum IUPAC Adsorption Isotherm Models Employing Sensitivity of Parameters for Rigorous Adsorption System Performance Evaluation. *Energies* **2021**, *14* (22), 7478. https://doi.org/10.3390/en14227478.
(60) Sing, K. S. W. Reporting Physisorption Data for Gas/Solid Systems with Special Reference to the Determination of Surface Area and Porosity (Recommendations 1984). *Pure and Applied Chemistry* **1985**, *57* (4), 603–619. https://doi.org/10.1351/pac198557040603.
(61) Küçük, İ.; Önal, Y. Synthesis, Characterization, and Adsorption Properties of Highly Microporous Structured Activated Carbon. *Journal of the Turkish Chemical Society Section A: Chemistry* **2021**, *8* (3), 821–834. https://doi.org/10.18596/jotcsa.753579.
(62) Yagmur, E.; Gokce, Y.; Tekin, S.; Semerci, N. I.; Aktas, Z. Characteristics and Comparison of Activated Carbons Prepared from Oleaster (Elaeagnus Angustifolia L.) Fruit Using KOH and ZnCl2. *Fuel* **2020**, *267*, 117232. https://doi.org/10.1016/j.fuel.2020.117232.

(63) Juan, Y.; Ke-qiang, Q. Preparation of Activated Carbon by Chemical Activation under Vacuum. *Environ. Sci. Technol.* **2009**, *43* (9), 3385–3390. https://doi.org/10.1021/es8036115.
(64) Allwar, A. Characteristics of Pore Structures and Surface Chemistry of Activated Carbons by Physisorption, Ftir And Boehm Methods. *IOSRJAC* **2012**, *2* (1), 09–15. https://doi.org/10.9790/5736-0210915.
(65) Tan, C. S.; Leow, S. Y.; Ying, C.; Tan, C. J.; Yoon, T. L.; Jingying, C.; Yam, M. F. Comparison of FTIR Spectrum with Chemometric and Machine Learning Classifying Analysis for Differentiating Guan-Mutong a Nephrotoxic and Carcinogenic Traditional Chinese Medicine with Chuan-Mutong. *Microchemical Journal* **2021**, *163*, 105835. https://doi.org/10.1016/j.microc.2020.105835.
(66) Valdés Renteria, C. F.; Betancur Guerrero, Y.; López López, D. P.; Gómez Gutiérrez, C. A.; Chejne Janna, F. Effects of Pyrolysis Atmosphere on the Porous Structure and Reactivity of Chars from Middle and High Rank Coals. *Ing. Inv.* **2018**, *38* (1), 31–45. https://doi.org/10.15446/ing.investig.v38n1.64516.
(67) Knauer, K. M.; Higginson, C.; Lee, M. Circular Plastics Technologies: Pyrolysis of Plastics to Fuels and Chemicals. *Physical Sciences Reviews* **2023**, *0* (0). https://doi.org/10.1515/psr-2022-0175.
(68) Sing, K. S. W.; Williams, R. T. Empirical Procedures for the Analysis of Physisorption Isotherms. *Adsorption Science & Technology* **2005**, *23* (10), 839–853. https://doi.org/10.1260/026361705777641990.
(69) Borrego, A. G.; Alvarez, D. Comparison of Chars Obtained under Oxy-Fuel and Conventional Pulverized Coal Combustion Atmospheres. *Energy Fuels* **2007**, *21* (6), 3171–3179. https://doi.org/10.1021/ef700353n.
(70) Islam, M.; Lantada, A. D.; Mager, D.; Korvink, J. G. Carbon-Based Materials for Articular Tissue Engineering: From Innovative Scaffolding Materials toward Engineered Living Carbon. *Adv Healthcare Materials* **2022**, *11* (1), 2101834. https://doi.org/10.1002/adhm.202101834.
(71) Minuto, F. D.; Policicchio, A.; Aloise, A.; Agostino, R. G. Liquid-like Hydrogen in the Micropores of Commercial Activated Carbons. *International Journal of Hydrogen Energy* **2015**, *40* (42), 14562–14572. https://doi.org/10.1016/j.ijhydene.2015.07.029.
(72) Adsorption at the Solid-Gas Interface. In *Fundamentals of Interface and Colloid Science*; Elsevier, 1995; Vol. 2, pp 1-1-1–118. https://doi.org/10.1016/S1874-5679(06)80004-8.